

Hyperboloidal slices for the wave equation of Kerr-Schild metrics and numerical applications

Michael Jasiulek

Abstract.

We present new results from two open source codes, using finite differencing and pseudo-spectral methods for the wave equations in (3+1) dimensions. We use a hyperboloidal transformation which allows direct access to null infinity and simplifies the control over characteristic speeds on Kerr-Schild backgrounds. We show that this method is ideal for attaching hyperboloidal slices or for adapting the numerical resolution in certain spacetime regions. As an example application, we study late-time Kerr tails of sub-dominant modes and obtain new insight into the splitting of decay rates. The involved conformal wave equation is freed of formally singular terms whose numerical evaluation might be problematically close to future null infinity.

1. Introduction

In the recent past, since the work of [1, 2, 3], hyperboloidal slicings have been used frequently for numerical computations in general relativity as an elegant solution to the outer boundary and the radiation extraction problem by including null infinity in the slicing [4]. The applications range from time-domain simulations of the scalar wave equation on Minkowski, Schwarzschild [3, 5] and Kerr background [6, 7] to compute quasi-normal mode oscillations, to study the late time behaviour of the solution, to study the influence of non-linear source terms, to compute the scalar self-force of point particles orbiting a Schwarzschild black hole [8] and to compute gravitational waveforms from extreme-mass-ratio inspirals [9, 10]. A new and interesting idea is to apply the framework to perturbation equations in the frequency domain [11]. Recently, the use of hyperboloidal slices even allowed to evolve the Einstein equations in axisymmetry including null infinity, see [12] and references therein.

The spatial domain in the numerical solution of hyperbolic PDEs is typically truncated at a finite coordinate distance where artificial outer-boundary conditions are imposed and the outgoing radiation of the test field is extracted. This practice causes certain well-known conceptual and practical difficulties such as artificial reflections on the outer-boundary which can destroy relevant features of the solution. In this context, the use of hyperboloidal slicings offers an alternative by including the physical boundary \mathcal{I}^+ on the numerical grid.

Many numerical applications require a specific coordinate system in a compact domain and it is necessary to attach hyperboloidal coordinates at some transition point. In the original work of [1] this was accomplished by introducing a transition zone, which required the fine-tuning of many parameters for the chosen transition function and a disadvantageous hyperboloidal transformation which had a suitable asymptotic behaviour but caused the outgoing characteristic speed to drop in the transition region. This led to numerical problems in subsequent works [5, 6, 8]. In the recent work [10], appearing during the completion of this paper, the authors present a solution to the problem.

For this paper we developed a finite differencing (FD) and a pseudo-spectral (PS) code in (3+1) dimensions [13] to test a new hyperboloidal transformation that simplifies the control over characteristic speeds for the 1st-order reduced wave equation on Kerr-Schild backgrounds. Thereby we can avoid the above mentioned problem by requiring the outgoing characteristic speed to be invariant under the compactifying hyperboloidal transformation. We demonstrate that by performing a numerical comparison with the attached hyperboloidal slices as originally used in [1]. As an example application we investigate the late-time decay rates in Kerr at the horizon, finite radii and null infinity and study the m -dependence of the splitting of certain sub-dominant modes which was found in the numerical studies of [6, 7]. More technically, we remove formally singular terms that appear in the conformal wave equation that might numerically be problematic to evaluate at the outer boundary \mathcal{I}^+ , where the conformal factor vanishes. Our framework is general enough to cover metrics of the Kerr-Schild form. Thus, our approach could be applied in the numerical analysis of quasi-normal modes in Vaidya [14], and more generally, in time-dependent non-axisymmetric Kerr-Schild spacetimes.

The infra-structure and implementations we present here are comprehensive, allowing standard coordinates in the spacetime interior in (3+1), smooth matching of hyperboloidal slices and covering the large class of Kerr-Schild metrics with FD and PS techniques. A comparable work is [5] in which Minkowski and Schwarzschild backgrounds are treated on hyperboloidal slices in (3+1) with PS techniques using the aforementioned non-optimal transition zone.

The paper is organised in the following way. In Sec. (2) we introduce our notation and convention of Kerr-Schild metrics and the scalar wave equation. At next Sec. (3) we briefly explain the hyperboloidal method as well as the particular hyperboloidal transformation we employed. Then we compare the resulting characteristic coordinate speeds and the scalar curvature for matched hyperboloidal slices with other methods. In section (4) we apply our method to solve the scalar wave equation with finite differencing, explain implementational details and compare different matching methods numerically in Sec. (5). We then proceed to explain the pseudo-spectral code and use this on a single hyperboloidal domain (no matching) to study polynomial decay rates of sub-dominant modes on Kerr.

Note that we use a tilde as in \tilde{r} or $\tilde{g}^{\mu\nu}$ to denote compactified hyperboloidal coordinates and components of tensors. Conformally rescaled tensors are denoted by a superscript Ω as in ${}^\Omega l^\mu = l^\mu/\Omega$ or ${}^\Omega g^{\mu\nu} = g^{\mu\nu}/\Omega^2$. Derivatives wrt the Kerr-Schild radius r are denoted by a prime like $dh/dr = h'$ and wrt the rescaled radius \tilde{r} by a dot $dh/d\tilde{r} = \dot{h}$.

2. Wave equation in Kerr-Schild coordinates

2.1. Kerr-Schild metrics and Kerr metric

Kerr-Schild metrics are of the general form

$$g^{\mu\nu} = \eta^{\mu\nu} - 2V(t, x^i) l^\mu l^\nu, \quad (1)$$

where $\eta^{\mu\nu} = \text{diag}(-1, 1, 1, 1)$ is the flat metric, (t, x^i) are Kerr-Schild coordinates and l^μ is a null vector wrt $\eta^{\mu\nu}$ ($\Rightarrow g^{\mu\nu} l_\mu l_\nu = 0$) of the form

$$l^\mu = (-1, l^i), \quad k^\mu = (1, l^i) - 2V l^\mu \quad (2)$$

and k^μ is the second null vector normalized to $k^\mu l_\mu = 2$ ($\Leftrightarrow l^i l^j \delta_{ij} = 1$). l^i and V ‡ are free functions that characterise the Kerr-Schild metric in question.

‡ We assume asymptotic flatness such that $V = M/r(1 + V_1/r + \mathcal{O}(1/r^2))$ and $l^i n_i = 1 + n \cdot l_1/r + \mathcal{O}(1/r^2)$, $n^i = x^i/r$. In Kerr for example $V = M/r(1 + \mathcal{O}(1/r^2))$ and $n \cdot l = 1 - a^2/2(1 - (n_z)^2)/r^2 - \mathcal{O}(1/r^4)$.

In Kerr with mass M and angular momentum aM we have

$$V(x^i) = M \frac{r_{\text{BL}}}{s} \quad (= \frac{M}{2} \nabla_\mu l^\mu), \quad (3)$$

where $s := \sqrt{(r^2 - a^2)^2 + (2az)^2}$, $r_{\text{BL}} = \frac{1}{\sqrt{2}} \sqrt{r^2 - a^2 + s}$ is the Boyer-Lindquist radius and $r = \sqrt{x^2 + y^2 + z^2}$ the Kerr-Schild radius, and

$$l^i = \left(\frac{r_{\text{BL}}x + ay}{r_{\text{BL}}^2 + a^2}, \frac{r_{\text{BL}}y - ax}{r_{\text{BL}}^2 + a^2}, \frac{z}{r_{\text{BL}}} \right). \quad (4)$$

Then $(-l^\mu)$ is the future directed ingoing principal null vector and k^μ the outgoing one. With our sign convention

$$n \cdot l = + \frac{r_{\text{BL}}}{r}, \quad (5)$$

where $n \cdot l := n_\mu l^\mu$, $n_i = n^i = x^i/r$ is the radial unit normal. Note that l^μ is affinely parametrised, i.e. $l^\mu \nabla_\mu l^\nu = 0$. Sometimes it can be useful to work with $\hat{l}^\mu := \sqrt{2V} l^\mu$. Then $\hat{l}^\mu \nabla_\mu \hat{l}^\nu = \phi \hat{l}^\nu = \partial_t V l^\nu = M \frac{a^2 - r^2}{s^2} \sqrt{\frac{1}{2V}} \hat{l}^\nu$.

2.2. Wave equation in 1st-order form

The hyperboloidal method, explained in the next section, includes a conformal rescaling of the metric. Therefore, we consider the conformal wave equation instead of $\square \Psi = 0$ §.

We reduce the conformal wave equation

$$(\square - \frac{1}{6} \mathcal{R}) \psi = g^{\mu\nu} \partial_\mu \psi_\nu - \Gamma^\mu(g) \psi_\mu - \frac{1}{6} \mathcal{R} \psi = 0 \quad (6)$$

to 1st-order form by introducing the new variables $\psi_\nu := \partial_\nu \psi$, where $\Gamma^\lambda(g) := g^{\mu\nu} \Gamma_{\mu\nu}^\lambda$ are the contracted Christoffel symbols and \mathcal{R} the scalar curvature of $g^{\mu\nu}$. In general $\Gamma^\mu = (\nabla_\mu \hat{l}^\mu + \phi) \hat{l}^\mu$ holds for metrics of the form (1). In Kerr it can be shown that

$$\Gamma^\mu(g) = \frac{2M}{s} l^\mu. \quad (7)$$

This leads to the following system of evolution equations for the variables $\{\psi_{\nu=0,1,2,3}, \psi\}$: $\partial_0 \psi = \psi_0$, $\partial_0 \psi_j = \partial_j \psi_0$ and

$$-g^{00} \partial_0 \psi_0 = 2g^{0i} \partial_i \psi_0 + g^{ij} \partial_i \psi_j - \Gamma^\mu(g) \psi_\mu - \frac{1}{6} \mathcal{R} \psi \quad (8)$$

which is symmetric hyperbolic. For finite-differencing implementations of (8) the following flux-conservative form is more convenient for long-term stability of the numerical evolution

$$-g^{00} \partial_0 \psi_0 = g^{0i} \partial_i \psi_0 + \frac{1}{\sqrt{g}} \partial_i F^i - \frac{1}{6} \mathcal{R} \psi \quad \text{where} \quad (9)$$

$$F^i := \sqrt{g} (g^{0i} \psi_0 + g^{ij} \psi_j). \quad (10)$$

where finite differences are taken of ψ_0 and F^i instead of differentiating the evolution variables ψ_0 and ψ_i directly. This, in turn, is more efficient if spectral methods are used to compute spatial derivatives and eq. (8) is preferred in that case.

§ The scalar wave equation $\square \psi = 0$ is per se not conformally invariant, i.e. a rescaled solution ${}^\Omega \psi := \psi/\Omega$ is in general not a solution of the wave eq. of the rescaled metric ${}^\Omega g^{\mu\nu} := g^{\mu\nu}/\Omega^2$, see for example appendix D of [15]. Note that $\mathcal{R} = 0$ holds for Kerr-Schild metrics where l^μ is geodesic like in Kerr or Vaidya spacetimes.

3. Hyperboloidal method

Having explained the wave equation on Kerr-Schild backgrounds we are now ready to describe the hyperboloidal method in the following section based on [1]. We explain the steps necessary to transform a given spacetime metric $g^{\mu\nu}$ in coordinates (t, x^i) and its t -slicing ($t = \text{const}$ hypersurfaces) to a conformal metric ${}^\Omega \tilde{g}^{\mu\nu}$ in radially compactified hyperboloidal coordinates (\tilde{t}, \tilde{x}^i) and its hyperboloidal \tilde{t} -slicing. It is often desirable to leave the coordinates (t, x^i) untouched in the spacetime interior, *inner domain*, and attach the *hyperboloidal domain* smoothly at some transition point r_{TR} . The hyperboloidal method we employ consist of three transformations, a radial compactification and a conformal rescaling of the metric

$$\tilde{x}^j = \Omega(r) x^j \quad \text{with} \quad \Omega = 0, \dot{\Omega} \neq 0 \text{ at } \mathcal{S}^+ \quad (11)$$

$${}^\Phi g_{\mu\nu} = \Phi^2 g_{\mu\nu} \quad \text{with} \quad \Phi \sim \Omega \text{ at } \mathcal{S}^+ \quad (12)$$

where $\dot{\Omega} := d\Omega/d\tilde{r}$ and we assume Ω and Φ non-negative. For simplicity we set $\Omega \equiv \Phi$ in the following, see Appendix B for $\Omega \neq \Phi$. The conformal transformation extends the spacetime to include \mathcal{S}^+ as its boundary [4] such that the conformal metric is regular there. For constant time slices to intersect \mathcal{S}^+ we require the additional transformation

$$\tilde{t} = t - h(r) \quad \text{with} \quad -\frac{I - 2n \cdot lV}{1 - 2n \cdot l^2 V} < h' < \frac{I + 2n \cdot lV}{1 - 2n \cdot l^2 V} \quad (13)$$

where the height function $h(r)$ possesses a carefully chosen asymptotic singular behaviour to allow \tilde{t} -slices to penetrate \mathcal{S}^+ , similar to time transformations from Schwarzschild slicing to horizon penetrating slicings, see for figure (2) in [16] for illustration purposes. The restrictions on $h(r)$ in (13) are necessary for the hyperboloidal slices to be spacelike, where $h' := dh/dr$ and $I := \sqrt{1 + 2V(1 - n \cdot l^2)}$.

3.1. Controlling the coordinate speed of in/outgoing characteristics

In numerical applications of the hyperboloidal method, like for the hyperbolic system (8), it is often necessary to limit the ratio $\frac{\Delta t}{\Delta r}$ to obtain a stable numerical evolution, where Δr is the spatial grid spacing and Δt the time step. This is the case, if the method of lines (MoL) and explicit time integration is used. Then the CFL-condition must hold $c(r) \frac{\Delta t}{\Delta r} \leq \nu_{\text{CFL}}$, where $c(r)$ is the coordinate speed of characteristics of the solution, explained in the following, and ν_{CFL} the so called Courant number that is independent of the solution. Therefore, an efficient numerical computation is limited by $\max c(r)$ and computing time may be wasted in regions where $c(r) < \max c(r)$. On the other hand it may be useful to obtain more temporal resolution in certain regions, for example to resolve a particular feature of the solution or to increase the accuracy there. In the following we bring the height function derivative $h'(r)$ in a particular form which allows to directly specify the outgoing characteristic speed $c(r)$ as a function of radius in the hyperboloidal transformation, i.e. $h'(r) \rightarrow h'(r, c(r))$ independently of Ω . We also show how to use this feature for attaching hyperboloidal slices to an inner domain ||.

The in/outgoing characteristic speeds in the direction n_i of a hyperbolic system of the form $\partial_t U = A^i \partial_i U + BU$, where we assume U is vector-valued and A^i, B are matrices, are

|| As mentioned in the introduction in the recent work [10] this problem is solved in a slightly different way. The authors do not explicitly consider the characteristic speeds but guarantee a smooth transition of inner and hyperboloidal coordinates through $t_{\text{BL}} - r_{\text{BL}}^* = \tilde{t} - \tilde{r}$, see eq.(7) of [10], where $t_{\text{BL}}, r_{\text{BL}}^*$ are the Boyer-Lindquist time and tortoise radius.

given by two eigenvalues of $A^i n_i$. For the systems (8), (9) they are

$$\begin{aligned} c^\pm(g) &:= \left(-g^{0n} \pm \sqrt{(g^{0n})^2 - g^{00} g^{nn}} \right) / (-g^{00}), \\ &= \frac{\pm I - 2Vn \cdot l}{1 + 2V} \xrightarrow{nl \rightarrow 1} \frac{+1 - 2V}{1 + 2V}; -1 \end{aligned} \quad (14)$$

where $g^{0n} = g^{0i} n_i$. We considered the limit $n \cdot l \rightarrow 1$ because in most parts of asymptotically flat spacetimes, see footnote 2, the two unit normals are almost aligned $n \cdot l \approx 1$, e.g. in extremal Kerr for $r > 1.2$. Instead of proceeding with the straightforward but long algebraic operations to simplify $c^\pm({}^\Omega \tilde{g})$, we proceed in a more intuitive way by considering the characteristic speeds of the 1st-order equation

$$l^\mu \partial_\mu \psi = 0 \quad (15)$$

which applies to the characteristics of the PDEs (8), (9). Characteristics propagate on null rays of the background along which the solution is constant. The radial characteristic speeds of eq. (15) along the null vectors $(-l^\mu)$, k^μ eq. (2) are

$$c^{(k)} = k^i n_i / k^0 = n \cdot l \frac{1 - 2V}{1 + 2V} \xrightarrow{nl \rightarrow 1} c^{(k)} \equiv c^+(g), \quad (16)$$

$$c^{(l)} = l^i n_i / l^0 = -n \cdot l \xrightarrow{nl \rightarrow 1} c^{(l)} \equiv c^-(g). \quad (17)$$

Under the compatifying hyperboloidal transformations (11),(13) $c^{(k)}$, $c^{(l)}$ change as

$$c^{(\tilde{k})} = n \cdot l \frac{1 - 2V}{1 + 2V} \frac{\Omega^2 L}{1 - h' \frac{1 - 2V}{1 + 2V} n \cdot l} \xrightarrow{nl \rightarrow 1} c^{(\tilde{k})} \equiv c^+(\tilde{g}), \quad (18)$$

$$c^{(\tilde{l})} = -n \cdot l \frac{\Omega^2 L}{1 + h' n \cdot l} \xrightarrow{nl \rightarrow 1} c^{(\tilde{l})} \equiv c^-(\tilde{g}), \quad (19)$$

where $L := \frac{\tilde{r}'}{\Omega^2} = \frac{1}{\Omega - \Omega \tilde{r}}$. From eq. (19) we can see that the conditions (11) on Ω , $\tilde{\Omega}$ make $c^{(\tilde{l})}$ vanish at \mathcal{S}^+ (no ingoing characteristics). Eq. (18) shows that to make $c^{(\tilde{k})}$ non-vanishing at \mathcal{S}^+ , h' has to be of the form

$$h' = \frac{1 + 2V}{1 - 2V} (1 - \Omega^2 L H) \xrightarrow{h' = h'(r)} \frac{1 + 2\hat{V}(r)}{1 - 2\hat{V}(r)} (1 - \Omega^2 L H(r)), \quad (20)$$

where $\hat{V}(r)$ is $V(x^i)$ along some arbitrary direction or some approximation. For practical purposes it is enough to consider the leading order term of $V(x^i)$, i.e. $\hat{V}(r) = 2M/r$, as we do in the following. H is a free function in the range from zero to one to modify the coordinate speeds in the hyperboloidal domain. The spacelike condition eq. (13) is guaranteed by h' of the above form, since $LH > 0$ by definition ¶. A simple choice might be $H = 1$. However, H allows direct access to the characteristic speed $c^{(\tilde{k})} = (1 - 2V)/(1 + 2V) 1/H$ eq. (18) and it is more convenient to require

$$c^{(\tilde{k})} = c^{(k)} \xrightarrow{nl \rightarrow 1} H(\tilde{r}) = \frac{1 - 2\hat{V}(r)}{1 + 2\hat{V}(r)} \cdot \frac{1 + 2\hat{V}(\tilde{r})}{1 - 2\hat{V}(\tilde{r})}. \quad (21)$$

This condition is the core of our hyperboloidal method. It ensures that the outgoing characteristic speed is unchanged under the compatifying hyperboloidal transformation, see

¶ One may object that for h' of (20) in the limit $\Omega \rightarrow 0$ $\frac{1 + 2M/r}{1 - 2M/r} < h'$. By expanding this inequality in Ω at 0 it becomes clear that this can only be if $LH < 0$.

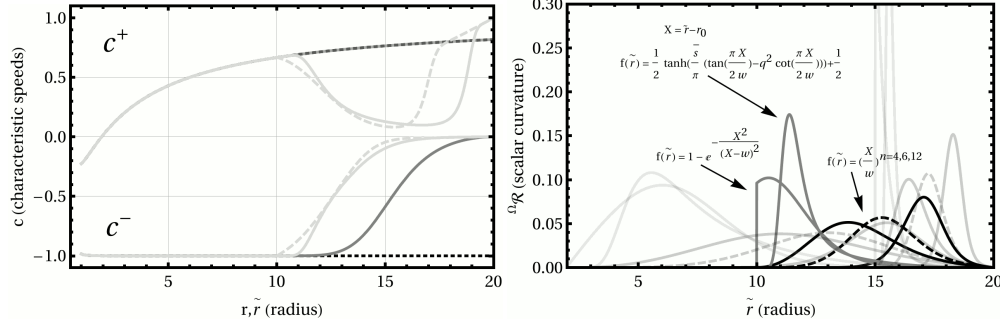


Figure 1. Left: Characteristic speeds c^\pm of the systems (8), (9) for Kerr $a = 0.5$ on t -slices (black dotted) $r \in [2; 20]$ and compactified hyperboloidal \tilde{t} -slices with $\tilde{r}|_{\mathcal{S}^+} = 20$ attached at $r_{\text{TR}} = 10$ for the hyperboloidal matching condition (21) (gray) and for (23) with $C = 20$ of Refs. [1, 5, 6, 8] (light gray) for transition functions f -tanh-tan (light g. solid) with $q = 1, \bar{s} = 2$ [5, 8] and f -exp (light g. dashed) [6, 1].

Right: $\Omega_{\mathcal{R}}(\tilde{r})$ for the conformal factors (transition functions $f(\tilde{r})$) of Refs. [1, 5, 6, 8] (gray) and our choice (black, $k = 6$ dashed). The same five curves are shown in two light gray groups for shifted transition points $r_{\text{TR}} = 2; 15$.

Fig. (1) (left) (gray curve overlapping black dotted curve), independent of the choice for Ω . We set Ω in the following to be

$$\Omega(\tilde{r}) = 1 - f(\tilde{r}) \quad \text{with} \quad f(\tilde{r}) = \left(\frac{X}{w}\right)^k \Theta(X), \quad X = \tilde{r} - \tilde{r}_{\text{TR}}, \quad (22)$$

where \tilde{r}_{TR} is the transition point and w the width of the hyperboloidal domain.

In the original work [1] and also adapted by [5, 6, 8] the height function derivative was set to

$$h' = f H_{\text{ext}} = f \left(1 + \frac{4M}{r} + \frac{(8M^2 - C^2)}{r^2} \right) \quad (23)$$

where C is a parameter and f ranging from zero to one a transition function and the conformal factor was set to $\Omega(\tilde{r}) = 1 - f(\tilde{r}) \frac{\tilde{r}}{S}$, $S = \tilde{r}|_{\mathcal{S}^+}$. H_{EXT} has the correct asymptotic singular behaviour, where $c^+|_{\mathcal{S}^+} = S^2/C^2$ but the characteristic speed in the hyperboloidal domain is left uncontrolled in the transition zone and depends on the details of f (as the spacelike condition (13)). In this case $c^{(\tilde{k})}$, see eq. (18), drops like Ω^2 before h' in the denominator sets in to result in a non zero $c^{(\tilde{k})}$ asymptotically. This effect is apparent in Fig. (1) (left) (light gray, light gray dashed), where we plotted c^\pm (14) for our choice (20), (21) and for (23) as in Refs. [1, 5, 6, 8].

4. Wave equation on hyperboloidal slicing

In the following we derive the explicit expressions for ${}^\Omega \tilde{g}^{\mu\nu}$, ${}^\Omega \mathcal{R}$ and $\Gamma^\mu({}^\Omega \tilde{g})$ that appear in the conformal wave eq.(6) under the compatifying conformal hyperboloidal transformations (11),(12),(13). We identify all formally singular terms which could constitute potential obstacles for numerical evaluations at the outer boundary \mathcal{S}^+ .

4.1. Transformation of the Kerr-Schild metric $g^{\mu\nu}$ and \mathcal{R} , Γ^μ

The metric components $g^{0\mu}$, g^{ij} and the determinant of $g^{\mu\nu}$ transform in a straightforward manner, divergent terms cancel trivially, the expressions are given in Appendix A. The

regularity of

$${}^{\Omega}\tilde{g}^{00} = (1 - 2n \cdot l^2 V) \left(\frac{h' - K_+}{\Omega^2} \right) (h' - K_-), \quad K_{\pm} = \frac{\pm I + 2n \cdot lV}{1 - 2n \cdot l^2 V} \quad (24)$$

at \mathcal{S}^+ is guaranteed by the form of h' in eq. (20), since $\frac{1-2M/r}{1+2M/r}K_+ =: 1 + \frac{1}{r^2}G \xrightarrow{r \rightarrow \infty} 1$ in asymptotically flat spacetimes⁺ and we obtain

$${}^{\Omega}\tilde{g}^{00} = (1 - 2n \cdot l^2 V) \frac{1 + 2M/r}{1 - 2M/r} \left(-HL - \frac{1}{\tilde{r}^2} G \right) (h' - K_-). \quad (25)$$

The scalar curvature ${}^{\Omega}\mathcal{R}$ of ${}^{\Omega}g^{\mu\nu}$ is given by

$${}^{\Omega}\mathcal{R} = -\frac{6}{\tilde{r}} \left((1 - 2n \cdot l^2 V)N + \dot{\Omega}L(3 - 2V) - \dot{\Omega}L\tilde{r} {}^{\Omega}\gamma_{n \cdot l} \right), \quad (26)$$

$${}^{\Omega}\mathcal{R} = -\frac{6}{\tilde{r}} \left((1 - 2n \cdot l^2 V)N + \dot{\Omega}L(3 - 4V) \right) \text{ for Kerr}, \quad (27)$$

$$N := \frac{1}{\Omega^2} (\Omega''r - \Omega') = (\ddot{\Omega}\Omega^2\tilde{r}L - \dot{\Omega}(\Omega - 3\dot{\Omega}\tilde{r}))L^2,$$

where ${}^{\Omega}\gamma := \gamma/\Omega$ depends on the Kerr-Schild metric in question. In Kerr $\gamma = 2M/s$, compare with (7). In certain cases it is useful to distinguish the conformal factor Φ and the rescaling factor Ω , then \mathcal{R} changes as in Appendix B. Besides h' , the conformal factor has to be picked carefully to avoid steep gradients in ${}^{\Omega}\tilde{g}^{\mu\nu}$ and ${}^{\Omega}\mathcal{R}$ (which appear on the rhs of eqs. (8),(9)) as shown in Fig. (1) (right).

Next we derive the expressions for $\Gamma^{\mu}({}^{\Omega}\tilde{g})$, where we first consider the conformal transformation behaviour of $\Gamma^{\mu}(g)$ under eq. (12):

$$\begin{aligned} \Gamma^{\mu}({}^{\Omega}g) &= {}^{\Omega}\Gamma^{\mu}(g) + {}^{\Omega}C^{\mu}, \\ {}^{\Omega}C^{\mu} &= -2\dot{\Omega}L({}^{\Omega}n^{\mu} - 2n \cdot l {}^{\Omega}V l^{\mu}), \end{aligned} \quad (28)$$

where ${}^{\Omega}C^{\mu}$ is a tensor, ${}^{\Omega}\Gamma^{\mu}(g) = \Gamma^{\mu}(g)/\Omega^2$, ${}^{\Omega}n^{\mu} = (0, n^i)/\Omega$ and ${}^{\Omega}V = V/\Omega$.

The transformation of $\Gamma^{\mu}({}^{\Omega}g)$ to compactified hyperboloidal coordinates involves the Hessian of (11),(13). We obtain

$$\Gamma^{\mu}({}^{\Omega}\tilde{g}) = \tilde{\Gamma}^{\mu}({}^{\Omega}g) - \frac{\partial \tilde{x}^{\mu}}{\partial x^{\nu} \partial x^{\lambda}} {}^{\Omega}g^{\nu\lambda} \quad (29)$$

$$\begin{aligned} \frac{\partial \tilde{x}^{\mu}}{\partial x^{\nu} \partial x^{\lambda}} {}^{\Omega}g^{\nu\lambda} &= \frac{1}{\Omega^2} \{ -h''(1 - 2n \cdot l^2 V) + 2h' \frac{1}{r} V(1 - n \cdot l^2) - 2h' \frac{1}{r}, \\ & n^i ((\Omega''r - \Omega')(1 - 2n \cdot l^2 V) + \Omega'(5 - 2V)) - 4l^i \Omega' n \cdot lV \} \end{aligned} \quad (30)$$

$$\begin{aligned} \frac{\partial \tilde{x}^{\mu}}{\partial x^{\nu} \partial x^{\lambda}} {}^{\Omega}g^{\nu\lambda} &= \{ -L \frac{d}{d\tilde{r}} h'(1 - 2n \cdot l^2 V) + 2h' \frac{1}{\tilde{r}} {}^{\Omega}V(1 - n \cdot l^2) - 2h' \frac{1}{\Omega\tilde{r}}, \\ & n^i (N(1 - 2n \cdot l^2 V) + \dot{\Omega}L(5 - 2V)) - 4l^i \dot{\Omega}L n \cdot lV \}. \end{aligned} \quad (31)$$

A closer look at the time component $\Gamma^0({}^{\Omega}\tilde{g})$ reveals that the third term in eq. (31) is divergent. It cancels with $-2\dot{\Omega}L {}^{\Omega}\tilde{n}^0 = -2\dot{\Omega}L(-h'/\Omega)$ that appears through the coordinate transformation ${}^{\Omega}C^{\mu} \rightarrow {}^{\Omega}\tilde{C}^{\mu}$, see eq. (28). We remove these terms from ${}^{\Omega}H^{\mu} := \frac{\partial \tilde{x}^{\mu}}{\partial x^{\nu} \partial x^{\lambda}} {}^{\Omega}g^{\nu\lambda}$ and ${}^{\Omega}\tilde{C}^{\mu}$ and denote them as ${}^{\Omega}H_{\text{r}}^{\mu}$ and ${}^{\Omega}\tilde{C}_{\text{r}}^{\mu}$, where ${}^{\Omega}D^{\mu}$ is the remainder of the cancellation.

$$\Gamma^{\mu}({}^{\Omega}\tilde{g}) = {}^{\Omega}\tilde{\Gamma}^{\mu}(g) + {}^{\Omega}\tilde{C}_{\text{r}}^{\mu} - {}^{\Omega}H_{\text{r}}^{\mu} + {}^{\Omega}D^{\mu}, \quad (32)$$

$${}^{\Omega}D^{\mu} := \{ 2h' L \frac{1}{\tilde{r}}, 0, 0, 0 \}. \quad (33)$$

⁺ $\frac{1-2M/r}{1+2M/r}K_+ = 1 + \frac{4M}{r^2}(n \cdot l_1 + V_1) + \mathcal{O}(r^{-3})$ and in Kerr $\frac{1-2M/r}{1+2M/r}K_+ = 1 - \frac{4M}{r^3}(a^2(n_z)^2) + \mathcal{O}(r^{-4})$.

5. Numerical applications

We are now ready for a numerical application of the methods described in the last section. We solve the system (9) using a (3+1) finite differencing (FD) code on attached hyperboloidal slices using g as in eq. (21) and h' as in eq. (23) as most commonly used in the literature and compare the evolution of the numerical errors. Then we solve the system (8) using a pseudo-spectral evolution scheme in (3+1), which allows higher accuracy than the FD code, to obtain new insights into the splitting of the late time tails of the solution [6, 7] and confirm known results about polynomial decay rates at finite radii and \mathcal{I}^+ . We also inspect the late-time part of the solution at the horizon, where oscillations have been predicted [17, 18] but until now not regarded in numerical studies.

With both implementations we evolve non-stationary compactly supported initial data (ID) of the form $\psi(0, x^i) = 0$, $\psi_j(0, x^i) = 0$ and

$$\psi_0(0, \tilde{x}^i) = Y^{l_0 m}(\tilde{x}^i) e^{-(\tilde{r} - \tilde{r}_0)^2 / (2\sigma^2)} \text{ and of the form} \quad (34)$$

$$\psi_0(0, \tilde{x}^i) = e^{-(\tilde{x}^i - \tilde{x}_0^i)(\tilde{x}^j - \tilde{x}_0^j) \delta_{ij} / (2\sigma^2)}, \quad (35)$$

where $\sigma, \tilde{r}_0, \tilde{x}_0^i$ are parameters and $Y^{l_0 m}(\tilde{x}^i)$ are the spherical harmonics wrt \tilde{x}^i . We set the Kerr parameter $M = 1$ and define the local power index (LPI) to be $\text{LPI}([\psi]^{lm}) := d \text{Log} |[\psi]^{lm}| / d \text{Log} t$, where $[\psi]^{lm}$ is the lm -spherical harmonic component of the field wrt Kerr-Schild coordinates.

5.1. Finite differencing code

Our finite differencing code `LlamaWaveHyperboloidal` [13] is embedded in the `Cactus` parallelization framework [19]. We made use of the extension `Llama` [20] of the `Carpet` driver [21], which handles the domain decomposition of grids over processors and provides the required interpolation operations for boundary communication. The `Llama` code, comparable to the multiblock code of [22], allows to use a spherical grid with the ‘‘inflated cube’’ coordinates [23] in the angular directions, which consists of six overlapping coordinate patches each with two angular coordinates of the general form $\rho = \arctan(x^i/x^k)$, $i \neq k$. The finite differences are computed of ${}^\Omega \psi_0$ and ${}^\Omega \tilde{F}^i$ in the radial and angular coordinates, then transformed to a common Cartesian basis and input to the rhs of eq. (9). The discretization of the fluxes ${}^\Omega \tilde{F}^i$ instead of the evolution variables ψ_i is beneficial for a long-term stable evolution. If used on a single Cartesian grid, see for example [24] and references therein, the form of eq. (9) is a necessary condition for the FD scheme to conserve a certain discrete energy norm [25]. Since we compute non-Cartesian FDs and use multiple overlapping coordinate patches, we require additional Kreiss-Oliger type artificial dissipation [26] to guarantees long-term stability. We use the method-of-lines with 4th-order Runge-Kutta time integration, 6th-order FD operators and add 5th-order artificial dissipation *(except at the radial boundaries) to the rhs of the evolution eq. for ψ_0 .

5.1.1. FD code: Comparison of matching methods As a non-trivial test case we evolved off-centered Gaussian ID with $\tilde{x}_0^i = (2.4, 1.2, 1.1)$, $\sigma = 1$ on the dented \tilde{t} -slicing, see eq. (23), corresponding to the solid light gray curve in Fig. (1) (left) and on the smoother \tilde{t} -slicing, see eq. (21), corresponding to gray curve in Fig. (1) (left). We set the radial grid spacing to $\Delta \tilde{r} = 0.05$, the time step to $\Delta \tilde{t} = 0.04$ and the number of angular grid points per patch to $N_\sigma \times N_\rho = 41 \times 41$.

* This is different from the 6-patch-code of [22], where summation-by-parts FD and dissipation operations are used at grid and patch boundaries.

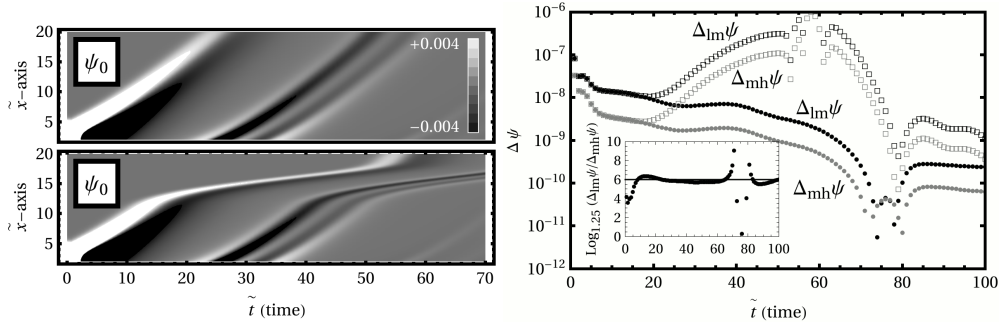


Figure 2. Left: Evolution of ψ_0 along \tilde{x} -axis for off-centered ID on dented hyperboloidal slicing (bottom) and smooth slicing (top) for Kerr $a = 0.1$. Slicing parameters and characteristic speeds as in Fig.(1) (left) light gray (f -tanh-tan) and gray curve (eq.(21)). The o . characteristic speed c^+ drops in the hyperboloidal domain which is apparent in the solution. Right: Evolution of the errors of ψ along \tilde{x} -axis for $l_0 = 0$ ID on dented slicing (squares) and smooth slicing (dots) for three resolutions $\Delta_{l,m,h} \tilde{t} = 0.0625, 0.05, 0.04$ with fixed $N_\rho = 41$. Inset: Convergence rate on smooth slicing.

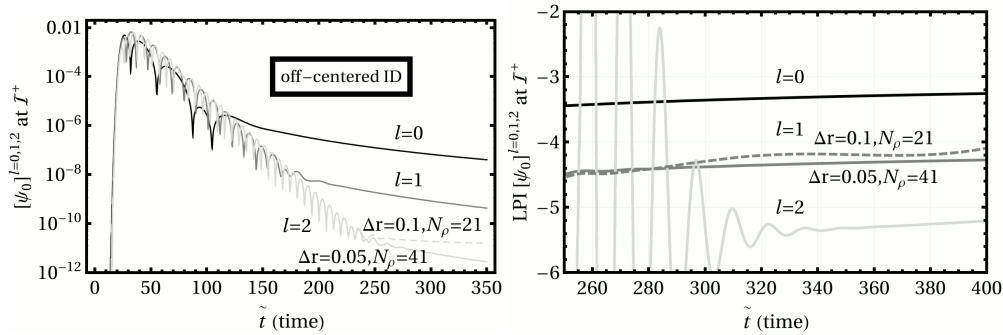


Figure 3. Evolution of the components $[\Psi_0]^{l=0,2,4}$ at \mathcal{I}^+ for off-centered ID on smooth hyperboloidal slicing. Setup as in Fig. (2) (left top). The field components decay at late times with a power law $\sim \tilde{t}^{-n}$ as apparent in the right plot. Sufficiently high resolution is necessary to see the correct power law at low amplitudes (dashed curves).

In Fig. (2) the outward propagation of the initial Gaussian pulse along the \tilde{x} -axis is shown. The pulse passes the transition point $r_{\text{TR}} = 10$ on the smooth slicing without apparent interferences (top panel). On the dented slicing (lower panel), the pulse slows down in agreement with c^+ of Fig. (1) (light gray) and leaves the numerical domain at later time. The larger gradients in the field at a given time, due to the bump in c^+ , cause the numerical error to be bigger as shown in Fig. (2) (right).

The decomposition of the field ψ_0 at \mathcal{I}^+ into spherical harmonics is shown in Fig. (3), an exponential oscillatory decay, followed by a polynomial decay with the asymptotic behaviour $\sim \tilde{t}^{-n}$ in agreement with the rule $n = l + 2$ for ψ , i.e. $n = l + 3$ for ψ_0 , derived analytically in [27] and confirmed in the recent numerical studies [6, 7]. We go into more detail about asymptotic decay rates in the next section, where we use pseudo-spectral methods and quad machine precision.

5.2. Spectral code

To resolve the late-time part of the solution higher numerical accuracy and machine precision is required than we are able to obtain with the FD implementation described in the last section, see Fig. (3). For this reason we created a code that uses spectral methods `SpectralWaveKerrHyperboloidal` [13] to compute spatial derivatives and the method of lines with 4th order Runge-Kutta time integration. In the spectral domain the evolution variables are expanded into real spherical harmonics Y^{lm} (angular direction) and Chebyshev polynomials C^n (radial direction), i.e. into the basis of polynomials $P^{lmn} := Y^{lm} C^n$, where we use Gauss-Legendre, Gauss-Lobatto collocation points, respectively. The hyperboloidal method in combination with horizon penetrating coordinates does not require any boundary treatment and unlike the FD implementation we use hyperboloidal slices that cover the whole numerical grid, i.e. beginning at the first, ending at the last collocation point, where we use as for the FD code the polynomial conformal factor (22) with $k = 6$, which is exactly represented in the coefficients space. If we wanted to use a hyperboloidal domain that covers the grid only partially, we would require two spectral domains that are joined at the transition point r_{TR} . Since the piecewise function Ω (22) defined on a single spectral domain contains the Heaviside function which is badly represented in the coefficients space.

The spherical harmonics and their derivatives $Y^{lm}, \partial_j Y^{lm}$ are expressed in Cartesian coordinates, similar to SpEC, see e.g. [28]. They are evaluated through another basis of harmonics $\Phi^{lm} = (n^j \mathcal{N}_j^{[lm]})^l$, where $\mathcal{N}_j^{[lm]}$ are constant complex null vectors $\mathcal{N}_i \mathcal{N}_j \delta^{ij} = 0$ labeled by l and m , spanning the $2l + 1$ harmonics in each l -eigenspace. We chose the same $\mathcal{N}_j^{[lm]}$ as in [29] such that the Y^{lm} and the Φ^{lm} are related by a Fourier transform in each l -eigenspace

$$Y^{lm} = B^{lm} \sum_{m'=-l}^l \Phi^{lm'} e^{-i m' m a_l}, \quad B^{lm} = (-1)^m \frac{1}{l!} \sqrt{\frac{(l+m)!(l-m)!}{4\pi(2l+1)}}, \quad (36)$$

where $a_l = 2\pi/(2l+1)$. The derivatives $\partial_j \Phi^{lm}$ take the simple form

$$\partial_j \Phi^{lm} = \partial_j n^i (n^k \mathcal{N}_k^{[lm]})^{l-1} l \mathcal{N}_j^{[lm]}, \quad (37)$$

where $\partial_j n^i = (\delta^{ij} - n^i n^j)/r$ and thus are tangential to the unit sphere. Given the decomposition of a function ψ into the polynomial basis P^{lmn} we obtain the tangential component of the derivative ${}^{\parallel}(\partial_j)\psi$ through $\partial_j Y^{lm} C^n$ and the radial component $\partial_r \psi$ through $Y^{lm} \partial_r C^n$ (or alternatively, through a recurrence relation for the Chebyshev coefficients). The complete partial derivative of ψ is then given by

$$\partial_j \psi = n_j \partial_r \psi + {}^{\parallel}(\partial_j)\psi. \quad (38)$$

Since we compute the rhs of eq. (8) in the physical space, we introduce an aliasing error which would cause high modes $> l_{\text{MAX}}$ to blow up during the evolution. For our implementation it was enough to erase the l_{MAX} -components of the rhs of ψ and ψ_0 at every step of the time integration to obtain a stable long term evolution and to leave the rhs of ψ_j untouched.

5.2.1. Spectral Code: Application to Late-time Decay Rates in Kerr A generic non-stationary compactly supported perturbation on Schwarzschild background decays at late times as t^{-n} , $n = 2l + 3$, Price [30]. On Kerr background the picture is more complicated. Since Kerr is not spherically symmetric, neighbouring l -modes are coupled. Until recently there was a controversy in the literature about the value of n for $l \geq 4$. In the simple picture the lowest l -mode (compatible with the azimuthal and equatorial symmetries of the ID) generated

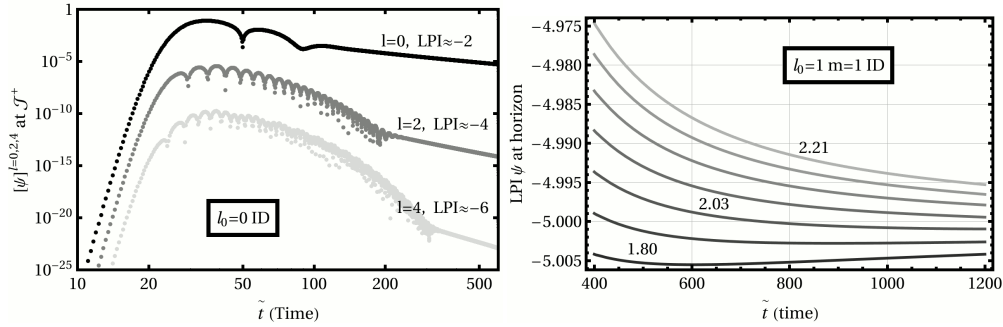


Figure 4. Left: Field components $[\psi]^l$ for l_0 ID in Kerr $a = 0.5$. The decay rates are in agreement with the rule $n = l + 2$. Right: LPI of ψ around the horizon between $\tilde{x}^i = (1.8 - 2.21, 0, 0)$ for $(l_0 = 1, m = 1)$ ID in Kerr $a = 0.1$ with $N_r = 90, N_\theta = 6$ grid points. The asymptotic decay rates approach $n = 5$ in agreement with $n = l_0 + l + 3$.

by mode mixing during the evolution is dominating the solution at late times. Nevertheless, analytical work by Hod [27], Barack and Ori [17] predict a surprising dependence of n (“memory effect”) on the initially excited mode l_0 , i.e. $n = n(l, l_0)$. By several numerical studies [28, 31, 32, 33] it was justified that both pictures are correct and that the decay rate depends on the details of the initial value formulation, i.e. the particular coordinates (Kerr-Schild, Boyer-Lindquist) in which the spherical harmonics are defined and the particular choice of initial data. Therefore, we distinguish between BL harmonics l_{BL} and KS harmonics l_{KS} in the following through subscripts, where necessary. Another effect that was predicted by Barack and Ori [17, 18] are oscillations on the late-time solution at the horizon (OAH).

Recently, the use of hyperboloidal slices in Kerr allowed Zenginoğlu and Tiglio [6] to extend these numerical investigation of polynomial decay rates at finite radii to future null infinity (compactly supported non-stationary ID $l_0 < 5$). Very recently, Racz and Toth [7] presented a more detailed study for various kinds of ID, including different fall-off properties towards null infinity up to $l_0 < 6$ where they investigated the behaviour of the sub-dominant modes as well (l -modes with decay faster than the slowest decaying mode). They could confirm numerically the m -independent rule, $n = l_0 + l + 3$ for $l \geq l_0$ and $n = l_0 + l + 1$ for $l < l_0$ proposed earlier by numerical studies [32, 33] which covers the formulas derived analytically in [27, 17]. For the late-time tails at \mathcal{S}^+ (TAS) the results of [6, 7] were found to fit the rule $n = l + 2$ for $l \geq l_0$ and $n = l_0$ for $l \leq l_0 - 2$ which has been obtained analytically in [27]. The authors of [7, 6] found a radial splitting of the decay rates for certain values of l_0, l and m , where the decay exponent varies for observers near the black hole, distant observers and at \mathcal{S}^+ . Moreover, the effect was found to depend on the harmonic index m [7]. We observe such a splitting in our simulations as well (SPL).

As an application of the hyperboloidal method we investigated the effects OAH, TAS, SPL on the late-time tails in Kerr. At first we check the convergence of the code for the non trivial test case of off-centered ID, see Fig. (6).

TAS: Fig. (4) (left) confirms that the late-time tail decay rates at \mathcal{S}^+ are in agreement with the rule $n = l + 2$, where the evolution of the $l = 0, 2, 4$ modes of ψ for $l_0 = 0$ initial data is shown.

OAH: In Fig. (4) (right) we show the LPI of ψ in the neighbourhood of the horizon between $\tilde{r} = 1.8 - 2.2$ (see figure). The field decays in agreement with the rule $n = l_0 + l + 3$ but no oscillations are present. The reason is the co-rotating azimuthal coordinate $\phi_+ =$

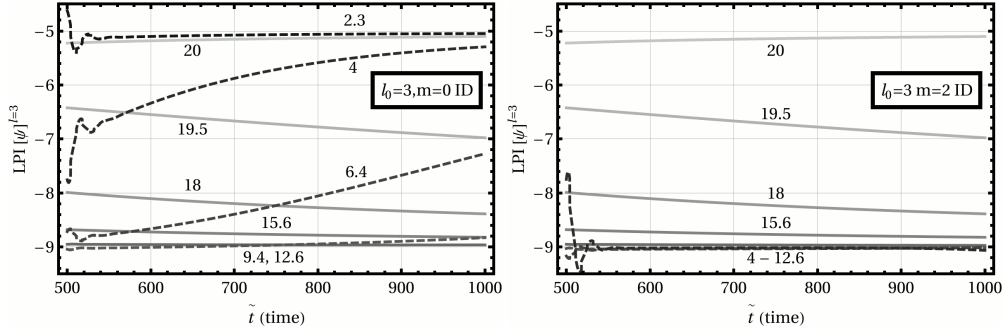


Figure 5. LPIs of $[\psi]^{l=3, m=0}$ (left) and $[\psi]^{l=3, m=2}$ (right) for $(l_0 = 3, m = 0, 2)$ ID at radii between $r = 2 - 12$ (dashed lines) and $r = 12 - 20$ (solid lines). Shown is the splitting, see text, of the LPIs at different radii for $m = 0$ compared to $m = 2$, where no splitting appears. For $N_r = 90$, $N_\theta = 7$ grid points and $a = 0.05$.

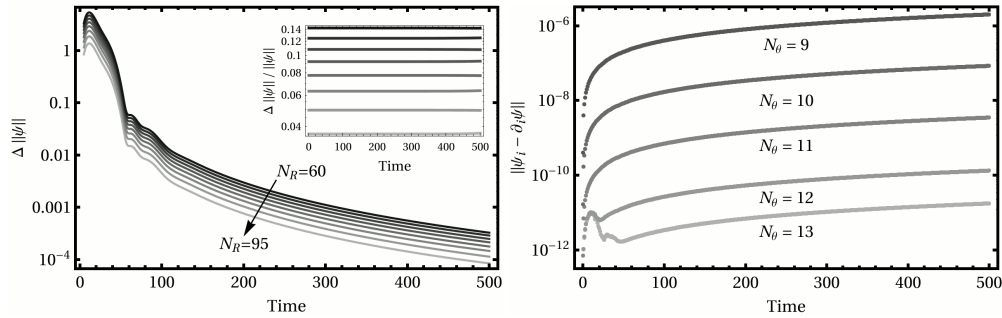


Figure 6. Left: Convergence of L_2 -norm of $\Delta\psi$ for off-centered ID with $N_r = 60, 65, 70, 75, 80, 85, 90, 95$, where $\Delta\psi$ is computed wrt $N_r = 110$. $a = 0.9$, $N_\theta = 10$, $\Delta t = 0.1$ are fixed. Right: Convergence of constraint field $\psi_i - \partial_i \psi$ at $N_\theta = 13, 12, 11, 10, 9$ with fixed $a = 0.9$, $N_r = 65$, $\Delta t = 0.1$.

$\phi_{\text{BL}} - t_{\text{BL}}\Omega_+$ ‡ used in [17, 18], where the Kerr-Schild $\phi_{\text{KS}} = \arctan y/x$ as $\tilde{\phi}$, which was used in [34], are independent of t_{BL} .

SPL: As we can see in Fig. (5) (left) the LPI of $[\psi]^{l=3, m=0}$ for $(l_0 = 3, m = 0)$ ID varies between $n = 5$ for $2 < \tilde{r} < 12$ (dashed), $n = 9$ for $12 < \tilde{r} < 20$ (solid) and $n = 5$ for $\tilde{r} = 20$ at \mathcal{S}^+ . We observed the same splitting for $(l_0 = 3, m = 1)$ ID (not shown). This effect is not present for $(l_0 = 3, m = 2)$ ID as shown in Fig. (5) (right) and for $(l_0 = 3, m = 3)$ ID (not shown). The reason is that Kerr-Schild $(l_0 = 3, m = 0, 1)$ ID as well as the examined l mode contain the $l_{\text{BL}} = 1$ harmonic which decays with $n = 1 + 1 + 3$. The ratio of the $l_{\text{BL}} = 1$ harmonic in the $l = 3$ Kerr-Schild mode decreases in the limits $a \rightarrow 0$ and $r \rightarrow \infty$, where we observe the field decaying with $n = 3 + 3 + 3$. It vanishes at \mathcal{S}^+ , where the BL and KS inclination coordinates agree and there the field decays like $n = 3 + 2$. By setting $m > 1$ we can exclude $l_{\text{BL}} = 1$ from the initial data and the splitting vanishes.

‡ According to [17, 18] the field decays at late times like $\sim t^{-n} e^{im\Omega_+ v(t, x^i)}$, where $v \sim t$ is the Eddington-Finkelstein null coordinate and $\Omega_+ = a/(2Mr_+)$, $r_+ = M + (M^2 - a^2)^{1/2}$.

6. Conclusion

We applied a compactifying conformal hyperboloidal (cch) transformation to the wave operator of Kerr-Schild metrics and derived all expressions, removed formally singular terms of the conformal wave equation for which the numerical evaluation at the outer boundary might be problematic. The hyperboloidal slices we used in that process let the outgoing characteristic speed invariant under the cch transformation independent of the Kerr-Schild metric in question. This was possible by analysing the characteristic speeds of the 1st-order reduced wave equation, whereby we obtained access to the arbitrary part H of the height function derivative for which the constraints on h' are automatically satisfied (suitable asymptotic behaviour, spacelike condition). This part allows to directly set the outgoing characteristic speed to the desired function of radius in the hyperboloidal domain eq. (21) and thereby to get more control on the efficiency and accuracy of the hyperboloidal method in numerical calculations, which we demonstrated through comparison with existing approaches in the literature. As an application we have numerically verified known decay rates of scalar test fields and their sub-dominant modes in Kerr at the horizon, finite radii and at \mathcal{I}^+ and obtained new insights into the m -dependence of the radial splitting of the late-time decay rates of certain harmonic modes.

The asymptotics of hyperboloidal slices simplify the boundary treatment in numerical simulations and provide a clean solution to the wave extraction problem. Moreover, the cch coordinate transformation beyond the boundary can act like an adaptive numerical grid on the background, i.e. H and Ω can be used to uniformly spread grid points or act as a magnifier to increase the spatial or temporal resolution, say in the neighbourhood of a localised source. In addition to providing that, the expressions presented here could lead to applications of the hyperboloidal approach to Kerr-Schild metrics beyond Kerr. The next step in improving the PS code would be to implement two spectral domains to be able to use piecewise defined conformal factors. It would be interesting to test the stability of the FD and PS code with non-linear source terms as in [5] or to use a localised moving effective source [8] to compute the scalar self-force on a particle orbiting a Kerr black hole and finally to extend the code to handle gravitational perturbations on Kerr-Schild backgrounds. The FD and PS code are available online [13].

Acknowledgments

It is a pleasure to thank Badri Krishnan, Anil Zenginoğlu, Frank Ohme, Barry Wardell, Alex B. Nielsen, José Luis Jaramillo, Gaurav Khanna, Leor Barack for useful discussions. I am grateful for advice from Ian Hinder and Daniela Alic on the long-term stability of FD codes, and from Nico Budewitz for technical support on the computer cluster at the AEI. I would also like to thank the many developers of the `Cactus`, `Carpet` and the `Llama` code and the very useful `SimFactor`. This work was supported by the IMPRS for Gravitational Wave Astronomy in the MPS.

Appendix A. Metric components ${}^{\Omega}\tilde{g}^{ij}$, ${}^{\Omega}\tilde{g}^{0j}$ and $\det {}^{\Omega}\tilde{g}_{\mu\nu}$

The cch transformation (11),(12),(13) change the metric components g^{0j} , g^{ij} of eq. (1) to

$${}^{\Omega}\tilde{g}^{0j} = {}^{\Omega}\tilde{\eta}^{0j} - 2{}^{\Omega}V \tilde{l}^0 \tilde{l}^j, \quad {}^{\Omega}\tilde{g}^{ij} = {}^{\Omega}\tilde{\delta}^{ij} - 2V {}^{\Omega}\tilde{l}^i \tilde{l}^j, \quad (\text{A.1})$$

$${}^{\Omega}\tilde{\eta}^{0j} = -h' L n^j, \quad {}^{\Omega}\tilde{\delta}^{ij} = \delta^{ij} + \tilde{r}\dot{\Omega}L(2 + \tilde{r}\dot{\Omega}L) n^i n^j, \quad (\text{A.2})$$

$$\tilde{l}^0 = l^0 - h' n \cdot l, \quad {}^{\Omega}\tilde{l}^i = l^i + n^i \tilde{r}\dot{\Omega}L n \cdot l, \quad (\text{A.3})$$

where ${}^\Omega V = V/\Omega$, in Kerr ${}^\Omega V = {}^\Omega r_{\text{BL}}/{}^\Omega s$ with ${}^\Omega s(\tilde{r}, \tilde{z}) = \Omega^2 s(\tilde{r}, \tilde{z}) = \sqrt{(\tilde{r}^2 - (\Omega\tilde{a})^2)^2 + (2\tilde{a}\Omega\tilde{z})^2}$ and ${}^\Omega r_{\text{BL}} = \frac{1}{\sqrt{2}}\sqrt{\tilde{r}^2 - \Omega^2\tilde{a}^2 + {}^\Omega s}$. The determinant is

$$\det g_{\mu\nu} = 1 \quad \rightarrow \quad \det {}^\Omega \tilde{g}_{\mu\nu} = 1/L^2. \quad (\text{A.4})$$

Appendix B. ${}^\Phi \mathcal{R}$ for $\Phi \neq \Omega$

In certain cases it can be useful to distinguish the conformal factor $\Phi = \Omega\lambda$ and the radial rescaling factor Ω , i.e. $\lambda \neq 1$, say if the metric should be left unchanged but the numerical grid has to be adapted in some region. In that case ${}^\Omega g^{\mu\nu} \rightarrow {}^\Omega \lambda g^{\mu\nu}$ in eq. (9) and ${}^\Phi \mathcal{R}$ becomes

$${}^\Phi \mathcal{R} = -\frac{6}{\lambda^3} \left[\frac{1}{\tilde{r}} \left((1 - 2n \cdot l^2 V) \hat{N} + L \dot{\Phi} (3 - 2V) \right) - L \dot{\Phi} n \cdot l^\Omega \gamma \right], \quad (\text{B.1})$$

$${}^\Phi \mathcal{R} = -\frac{6}{\lambda^3 \tilde{r}} \left[(1 - 2n \cdot l^2 V) \hat{N} + L \dot{\Phi} (3 - 4V) \right] \quad \text{in Kerr}, \quad (\text{B.2})$$

where $\hat{N} := \frac{1}{\Omega^2}(\Phi' r - \Phi') = L^2(L_1 \dot{\Phi} + \Omega \ddot{\Phi}) \tilde{r} - L \dot{\Phi}$, $L_1 := 2\dot{\Omega} + \ddot{\Omega} \tilde{r} L$. The conformal transformation $\Gamma^\mu({}^\Omega \tilde{g}) \rightarrow \Gamma^\mu({}^\Omega \lambda \tilde{g})$ of eq. (32) is given by

$$\Gamma^\mu({}^\Omega \lambda \tilde{g}) = {}^\Omega \tilde{\Gamma}^\mu(g)/\lambda^2 + {}^\Omega \tilde{C}_R^\mu - {}^\Omega H_R^\mu/\lambda^2 + {}^\Omega D^\mu, \quad (\text{B.3})$$

$${}^\Omega C^\mu = -2\dot{\Phi} L({}^\Omega n^\mu - 2n \cdot l^\Omega V l^\mu)/\lambda^2, \quad (\text{B.4})$$

$${}^\Omega D^\mu = \{2h' L \frac{1}{\tilde{r}} (\tilde{r} \dot{\lambda}/\lambda + 1), 0, 0, 0\}/\lambda^2. \quad (\text{B.5})$$

References

- [1] Anil Zenginoğlu. Hyperboloidal foliations and scri-fixing. *Class.Quant.Grav.*, 25:145002, 2008.
- [2] Anil Zenginoğlu. A Hyperboloidal study of tail decay rates for scalar and Yang-Mills fields. *Class.Quant.Grav.*, 25:175013, 2008.
- [3] Anil Zenginoğlu, Dario Nunez, and Sascha Husa. Gravitational perturbations of Schwarzschild spacetime at null infinity and the hyperboloidal initial value problem. *Class.Quant.Grav.*, 26:035009, 2009.
- [4] H. Friedrich. Cauchy problems for the conformal vacuum field equations in general relativity. *Communications in Mathematical Physics*, 91(4):445–472, 1983.
- [5] Anil Zenginoğlu and Lawrence E. Kidder. Hyperboloidal evolution of test fields in three spatial dimensions. *Phys.Rev.*, D81:124010, 2010.
- [6] Anil Zenginoğlu and Manuel Tiglio. Spacelike matching to null infinity. *Phys.Rev.*, D80:024044, 2009.
- [7] Istvan Racz and Gabor Zsolt Toth. Numerical investigation of the late-time Kerr tails. *Class. Quant. Grav.*, 28:195003, 2011.
- [8] Ian Vega, Barry Wardell, and Peter Diener. Effective source approach to self-force calculations. *Class.Quant.Grav.*, 28:134010, 2011.
- [9] Sebastiano Bernuzzi, Alessandro Nagar, and Anil Zenginoğlu. Binary black hole coalescence in the large-mass-ratio limit: the hyperboloidal layer method and waveforms at null infinity. 2011. * Temporary entry *
- [10] Anil Zenginoğlu and Gaurav Khanna. Null infinity waveforms from extreme-mass-ratio inspirals in Kerr spacetime. 2011. * Temporary entry *
- [11] Anil Zenginoğlu. A geometric framework for black hole perturbations. 2011. * Temporary entry *
- [12] Oliver Rinne. An Axisymmetric evolution code for the Einstein equations on hyperboloidal slices. *Class.Quant.Grav.*, 27:035014, 2010.
- [13] <https://bitbucket.org/mjasiulek>.
- [14] Cecilia Chirenti and Alberto Saa. Nonstationary regime for quasinormal modes of the charged Vaidya metric. *Phys. Rev.*, D84:064006, 2011.
- [15] Robert M. Wald. *General Relativity*. 1984. Book, The University of Chicago Press, 1984.
- [16] Anil Zenginoğlu. Asymptotics of black hole perturbations. *Class.Quant.Grav.*, 27:045015, 2010.
- [17] Leor Barack and Amos Ori. Late time decay of scalar perturbations outside rotating black holes. *Phys.Rev.Lett.*, 82:4388, 1999.
- [18] Leor Barack and Amos Ori. Late time decay of gravitational and electromagnetic perturbations along the event horizon. *Phys.Rev.*, D60:124005, 1999.

- [19] T. Goodale, G. Allen, G. Lanfermann, J. Massó, T. Radke, E. Seidel, and J. Shalf. The Cactus framework and toolkit: Design and applications. In *Vector and Parallel Processing – VECPAR'2002, 5th International Conference, Lecture Notes in Computer Science*, Berlin, 2003. Springer.
- [20] Denis Pollney, Christian Reisswig, Erik Schnetter, Nils Dorband, and Peter Diener. High accuracy binary black hole simulations with an extended wave zone. *Phys.Rev.*, D83:044045, 2011.
- [21] Erik Schnetter, Scott H. Hawley, and Ian Hawke. Evolutions in 3-D numerical relativity using fixed mesh refinement. *Class.Quant.Grav.*, 21:1465–1488, 2004.
- [22] Erik Schnetter, Peter Diener, Ernst Nils Dorband, and Manuel Tiglio. A Multi-block infrastructure for three-dimensional time-dependent numerical relativity. *Class.Quant.Grav.*, 23:S553–S578, 2006.
- [23] Jonathan Thornburg. Black hole excision with multiple grid patches. *Class.Quant.Grav.*, 21:3665–3692, 2004.
- [24] Gioel Calabrese and David Neilsen. Spherical excision for moving black holes and summation by parts for axisymmetric systems. *Phys. Rev.*, D69:044020, 2004.
- [25] B. Gustafsson, H.O. Kreiss, and J. Olinger. *Time dependent problems and difference methods*, volume 24. Wiley-Interscience, 1995.
- [26] H. Kreiss and J. Olinger. *Methods for the approximate solution of time dependent problems*. Number 10. Global Atmospheric Research Programme-WMO-ICSU Joint Organizing Committee, 1973.
- [27] Shahar Hod. Mode coupling in rotating gravitational collapse of a scalar field. *Phys.Rev.*, D61:024033, 2000.
- [28] Mark A. Scheel, Adrienne L. Erickcek, Lior M. Burko, Lawrence E. Kidder, Harald P. Pfeiffer, et al. 3-D simulations of linearized scalar fields in Kerr space-time. *Phys.Rev.*, D69:104006, 2004.
- [29] Michael Jasiulek. A New method to compute quasi-local spin and other invariants on marginally trapped surfaces. *Class.Quant.Grav.*, 26:245008, 2009.
- [30] Richard H. Price. Nonspherical perturbations of relativistic gravitational collapse. 1. Scalar and gravitational perturbations. *Phys.Rev.*, D5:2419–2438, 1972.
- [31] Manuel Tiglio, Lawrence E. Kidder, and Saul A. Teukolsky. High accuracy simulations of Kerr tails: Coordinate dependence and higher multipoles. *Class.Quant.Grav.*, 25:105022, 2008.
- [32] Lior M. Burko and Gaurav Khanna. Late-time Kerr tails: Generic and non-generic initial data sets, 'up' modes, and superposition. *Class.Quant.Grav.*, 28:025012, 2011.
- [33] Lior M. Burko and Gaurav Khanna. Late-time Kerr tails revisited. *Class.Quant.Grav.*, 26:015014, 2009.
- [34] William Krivan, Pablo Laguna, and Philippos Papadopoulos. Dynamics of scalar fields in the background of rotating black holes. *Phys.Rev.*, D54:4728–4734, 1996.